Article

Variation in InO Crystal Phase Alters Catalytic Performance toward the Reverse Water Gas Shift Reaction

Jianyang Wang, Chun-Yen Liu, Thomas P. Senftle, Jie Zhu, Guanghui Zhang, Xinwen Guo, and Chunshan Song

ACS Catal., **Just Accepted Manuscript** • DOI: 10.1021/acscatal.9b04239 • Publication Date (Web): 24 Dec 2019

Variation in In_2O_3 Crystal Phase Alters Catalytic Performance toward the Reverse Water Gas Shift Reaction

Jianyang Wang,[a‡] Chun-Yen Liu,[b‡] Thomas P. Senftle,[b] Jie Zhu,[a] Guanghui Zhang,[a*] Xinwen Guo,[a*] and Chunshan Song,[a,c*]

[a] State Key Laboratory of Fine Chemicals, PSU-DUT Joint Center for Energy Research, School of Chemical Engineering, Dalian University of Technology, Dalian 116024, P. R. China.

[b] Department of Chemical and Biomolecular Engineering, Rice University, Houston, TX 77005, United States.

[c] EMS Energy Institute, Department of Energy & Mineral Engineering and Chemical Engineering, PSU-DUT Joint Center for Energy Research, Pennsylvania State University, University Park, PA 16802, United States.

ABSTRACT: Understanding the structure-catalytic activity relationship is crucial for developing new catalysts with desired performance. In this contribution, we report the performance of In_2O_3 with different crystal phases in the reverse water gas shift (RWGS) reaction, where we observe changing activity induced by a phase transition under reaction conditions. Cubic In_2O_3 (c-In_2O_3) exhibits a higher RWGS rate than the hexagonal phase (h-In_2O_3) at temperatures below 350℃, due to its (1) enhanced dissociative adsorption of H_2, (2) facile formation of the oxygen vacancies, and (3) enhanced ability to adsorb and activate CO_2 on the oxygen vacancies, as suggested both experimentally and computationally. Density functional theory (DFT) results indicate that the surface oxygen arrangement on the cubic polymorph is key to rapid H_2 adsorption, which facilitates oxygen vacancy formation and subsequent CO_2 adsorption to yield high RWGS reactivity. At 450℃ and above, the activity of the h-In_2O_3 increases gradually with time on stream, which is caused by a phase transition from h-In_2O_3 to c-In_2O_3. In-situ XRD experiments show that h-In_2O_3 is first reduced by H_2, and subsequently oxidized by CO_2 to c-In_2O_3. These findings highlight the importance of the crystal phase in the catalytic RWGS reaction and provide a new dimension for understanding/designing RWGS catalysts.

KEYWORDS: *In_2O_3 catalysts, crystal phase transition, reverse water gas shift reaction, oxygen vacancy, DFT simulations, in-situ XRD*

INTRODUCTION

In recent years, with growing energy demand and the burning of fossil fuel, a considerable amount of CO_2 is emitted into the atmosphere leading to increasing global temperature and ocean acidification, posing threats to the world's ecosystems. Therefore, developing techniques for catalytic CO_2 reduction to make higher-value products, such as fuels or key molecular building blocks for the chemical industry, is a promising way to ameliorate this threat.[1-5] CO_2 hydrogenation to CO, commonly known as the reverse water gas shift (RWGS) reaction, can be coupled with other processes, such as Fischer-Tropsch synthesis, and thus has been extensively studied as a CO_2 mitigation strategy.[6-8] Among all known RWGS catalysts,[9-20] In-based catalysts have excellent performance due to the large number oxygen vacancies on the surface of these materials. Under methanol synthesis conditions, where shutting down RWGS was desirable, RWGS is inhibited on In_2O_3, and CO_2 does not adsorb and activate in oxygen vacancies in the cubic (110) surface.[21-22] However, under atmospheric pressure, CO is the main reaction product over In-based catalysts, instead of methanol. Liu et al. developed a deep understanding of In-based catalysts combining theoretical calculations and experimental investigations. They elucidated the critical role of the oxygen vacancy, and found the catalytic activity of In_2O_3 can be enhanced by mixing In_2O_3 with CeO_2 to promote the formation of oxygen vacancies.[23-24] In many cases, the activity is heavily affected by the support, the particle size, and the crystal structure of the catalysts.[25-26]

It has been previously shown that catalysts/supports with different crystal phases show remarkably different performance, including the reaction rate, selectivity, and stability.[27-31] Kim et al. prepared monodispersed RuO_2 nanoparticles supported on TiO_2, where the activity and product selectivity were strongly dependent on the TiO_2 crystal phases.[32] Song et al. also observed a similar phenomenon on Co/TiO_2 catalysts with different TiO_2 crystal phases exhibiting different performance for CO_2 methanation. The Co/rutile-TiO_2 catalyst selectively catalyzes CO_2 hydrogenation to CH_4, while CO is the main product on the Co/anatase-TiO_2 catalyst.[29] Based on a density functional theory (DFT)-based kinetic study, Li et al. found that CO activation on hexagonal close-packed (HCP) Co has much higher intrinsic activity than that of face centered-cubic (FCC) phase in Fischer-Tropsch synthesis, due to the presence of favorable active sites not available for FCC Co.[33] Nie et al. experimentally found that HCP-Co indeed exhibits higher activity toward hydrocarbon formation than FCC-Co.[34]

Crystalline In_2O_3 exists in two predominant polymorphs, the cubic (bixbyite type) and hexagonal (corundum type), and most of the studies have been focused, both experimentally and theoretically, on the cubic form.[23-24, 35-50] Hexagonal In_2O_3 (h-In_2O_3) has been studied far less than cubic In_2O_3 (c-In_2O_3).[51] In

this work, we compare the catalytic performance of c-In_2O_3 and h-In_2O_3 in RWGS reaction. c-In_2O_3 shows higher RWGS rate than h-In_2O_3 due to the facile formation of oxygen vacancies and stronger adsorption of CO_2. We also show that under certain reaction conditions, h-In_2O_3 transforms to c-In_2O_3 leading to increasing catalytic RWGS performance.

EXPERIMENTAL SECTION

Synthesis of In_2O_3: c-In_2O_3 was prepared through the controlled calcination of $In(OH)_3$.[48] Typically, 5.2 g of $In(NO_3)_3 \cdot 5H_2O$ was dissolved in 120 mL of deionized water, followed by the addition of NH_4OH (80 mL, 15 wt.% in H_2O). After centrifugation and decantation, the precipitate was collected and washed with deionized water. The c-In_2O_3 was obtained after drying the precipitate at 80 ℃ for 12 h, and calcination at 490 ℃ for 2 h with a ramping rate of 2 ℃/min in air. Prior to the RWGS reaction, the c-In_2O_3 was treated at 430 ℃ for 2h in mixture gas ($CO_2/H_2/N_2$= 28:56:16) at a flow rate of 60 mL/min.

h-In_2O_3 was prepared by a modified solvothermal reaction.[51] 40 mL of oleic acid, 20 mL of n-amyl alcohol and 80 mL of n-hexane were firstly mixed. 8 mL 0.5 mol/L $In(NO_3)_3$ and 8 mol/L NaOH solutions (volume ratio, v/v=1:1) were simultaneously added into this solution under vigorous stirring at 70 °C for 1h. The obtained emulsion was added into an autoclave and heated at 200 °C for 40 h, and then allowed to cool to room temperature. The precipitate was washed several times with absolute ethanol and deionized water, and then the sample was dried at 80 ℃ for 12 h, and calcined at 490 ℃ for 2 h with a ramping rate of 2 ℃/min in air. Prior to the RWGS reaction, the h-In_2O_3 was treated at 350 ℃ for 2h in mixture gas ($CO_2/H_2/N_2$= 28:56:16) at a flow rate of 60 mL/min.

Characterization. The X-ray diffraction (XRD) patterns of the fresh and spent catalysts were obtained using a Rigaku SmartLab 9kw diffractometer with Cu Kα radiation (λ = 1.5406 Å) with 0.02° step size over the range between 5° and 80°. In situ XRD measurements were performed in the XRK 900 reactor chamber made by Anton Paar Corporation. The catalyst powder was packed into the ceramic sample stage (internal diameter 15 mm). There are beryllium windows on the hermetic reactor chamber allowing the X-ray through. The temperature was controlled using a TCU 750 Temperature Control Unit. The XRD data were analyzed using the integrated PDXL2 software. The crystallite phases were identified by comparing the diffraction patterns with the data from the Joint Committee on Powder Standards (JCPDS) database.

The textural properties of the samples were determined by N_2 adsorption on a Quantachrome AUTO-SORB-1-MP sorption analyzer at liquid nitrogen temperature (-196 °C). The specific surface area was determined by the Brunauer-Emmett-Teller (BET) method. And the pore size distribution was obtained using the adsorption isotherm through Barrett-Joyner-Halenda (BJH) method. Prior to the measurements, the catalysts were treated under vacuum at 300 °C for 2 h.

Scanning electron microscopy (SEM) images were obtained on a Hitachi S-5500 instrument with an acceleration voltage of 3 kV. High-resolution TEM (HRTEM) imaging was conducted to obtain clear lattice fringes of the catalysts, and were taken on a Tecnai F30 HRTEM instrument (FEI Corp.) operated at 300 kV. The samples for TEM analysis were prepared by dropping ethanol suspension of samples on the carbon film-coated copper grids.

H_2 temperature-programmed reduction (H_2-TPR) was conducted on a Chem BET Pulsar TPR/TPD equipment (Quanta chrome, USA). About 100 mg of the sample was placed in a quartz tube in the furnace. To remove the moisture and other contaminants, the sample was flushed with He at 300 °C for 1 h, and then cooled to room temperature. The sample was reduced with 5 vol.% H_2/Ar at a flow rate of 30 mL/min, and heated to 800 °C with a ramp rate of 10 °C/min. For removal of the water formed during the reduction, a cooling trap was placed between the sample and the thermal conductivity detector (TCD). Temperature-programmed desorption of CO_2 (CO_2-TPD) was performed using the same instrument as the H_2-TPR. 200 mg of the sample was reduced in 5 vol.% H_2/Ar (30 mL/min) at 300 °C for 1 h, and then cooled to 50 °C, followed by CO_2 adsorption at 50 °C for 2 h. The sample was then flushed with N_2 with a flow rate of 30 mL/min, and heated to 700 °C at a ramp rate of 5 °C /min. Desorbed species were monitored by TCD (TPD) and mass spectrometry (TPD-MS).

X-ray photoelectron spectroscopy (XPS) analysis was performed over a spectrometer (Model Max 200, Leybold, Germany), using Al Kα radiation as an excitation source.

Catalytic Testing. The CO_2 hydrogenation performance over c-In_2O_3 and h-In_2O_3 were evaluated in a continuous-flow fixed-bed reactor under 0.1MPa (gauge pressure). The flow rate of the feed gas was controlled using a mass flow controller (Brooks 5850E). The reactor was heated by a Micrometrics Eurotherm 2416 furnace while the catalyst bed temperature was monitored using a K-type thermocouple located at the center of the catalyst bed. Prior to the catalytic test, the catalyst (0.2 g) was packed into a quartz reactor (inner diameter 6 mm) and purged with N_2 at a flow rate of 60 mL/min at target temperature for 30 min. Then, the feed gas was switched to the CO_2, H_2 and N_2 mixture gas ($CO_2/H_2/N_2$= 28:56:16) at a flow rate of 60 mL/min. The gas products were analyzed online using an Agilent 7890B gas chromatograph with a TDX-01 column connected to a TCD. The catalytic performance was evaluated by the conversion of CO_2 on the basis of the different concentrations between the inlet and outlet, which is defined as

$$x_{CO_2} = \frac{n_{CO_2}^{in} - n_{CO_2}^{out}}{n_{CO_2}^{in}} \times 100\% \quad (1)$$

the selectivity of CO and CH_4 are defined as follows:

$$S_{CO} = \frac{n_{CO}^{out}}{n_{CO}^{out} + n_{CH_4}^{out}} \times 100\% \quad (2)$$

$$S_{CH_4} = \frac{n_{CH_4}^{out}}{n_{CO}^{out} + n_{CH_4}^{out}} \times 100\% \quad (3)$$

where n_{CO}^{out}, $n_{CH_4}^{out}$, and $n_{CO_2}^{out}$ represent moles concentration of CO, CH_4 , CO_2 at the inlet and outlet of the reactor, and $n_{CO_2}^{in}$ is the moles concentration of CO_2 in the feed.

Density Functional Theory. Density functional theory (DFT) was implemented with the Vienna *ab initio* Simulation Package (VASP 5.4.4).[52] The projector augmented-wave (PAW) method was applied to treat core electrons with default potentials in VASP,[53-54] while the Perdew-Burke-Ernzerhof (PBE) exchange-correlation functional was employed with spin polarization.[55] The explicit valence electrons for each atom type were: C – $2s^2 2p^2$, H – $1s^1$, In – $5s^2 4d^{10} 5p^1$, and O – $2s^2 2p^4$. Monkhorst-Pack (MP) k-point mesh samplings were 2×2×1 for the c-In_2O_3(111) surface model and 3×3×1 for h-In_2O_3(110)

surface model.[56] Each facet was chosen because it is the most thermodynamically stable facet of each phase,[57] which is also reflected in the XRD analysis in **Figure 1a**. Plane wave basis sets were truncated at a kinetic energy cutoff of 700 eV, where Gaussian smearing was applied with 0.05 eV width. A self-consistent dipole correction perpendicular to the In_2O_3 surfaces was applied, as implemented in VASP. Geometries were optimized until forces converged to 0.05 eV/Å. The Grimme-D3 dispersion correction was included to treat van der Waals interactions.[58] Surface models included three layers of c-In_2O_3(111) and h-In_2O_3(110), where all layers were relaxed to avoid generating dipoles that can arise when freezing oxide layers on the reverse side of the slab.[59] The distance between the substrates in the periodic cell is at least 15 Å in the z direction. The energies of O_2, H_2, CO_2, CO, and H_2O were calculated in a 15×16×17 $Å^3$ simulation cell with 1×1×1 MP sampling. Since DFT with generalized gradient approximation (GGA) functionals are known to describe localized electrons incorrectly, we also tested the sensitivity of our results with respect to Dudarev's DFT+U formalism.[60] For these tests we employed a U value of 7 eV on the d electrons of In.[61] We found that the +U correction did not alter trends between the various In_2O_3 surfaces but did systematically shift adsorption energies. As such, both DFT and DFT+U adsorption energies are discussed in the Results section.

Translational, rotational, and vibrational entropy corrections were computed using standard formulae derived from statistical mechanics, while only vibrational entropy was included for adsorbed species with no translational or rotational degrees of freedom. Most structures were confirmed to be true energy minima with no imaginary vibrational modes present after a frequency analysis with finite differences of 0.02 Å. Only one structure (hydrogen adsorbed on the h-In_2O_3(110) surface) had a recalcitrant imaginary frequency of 196.47 cm^{-1} that could not be removed despite repeated optimization attempts with tighter convergence criteria (from 0.05 eV/Å to 0.01 eV/Å), which we attribute to numerical noise. Details for accessing an online repository containing all coordinates for optimized structures and total DFT energies are provided in the SI.

Oxygen vacancy formation energy (ΔE_{Ovac}) and hydrogen adsorption energy (ΔE_{Hads}) at all surface sites were computed by **Equations 4** and **5**, respectively, where $E_{In_2O_3}$ is the total DFT energy of the clean surface, $E_{In_2O_3-vac}$ is the total DFT energy of the surface with one oxygen vacancy, E_{O_2} is the total DFT energy of the oxygen molecule, $E_{H-In_2O_3}$ is the total DFT energy of the surface with one adsorbed hydrogen atom, and E_{H_2} is the total DFT energy of the hydrogen molecule.

$$\Delta E_{Ovac} = E_{In_2O_3-vac} + \frac{1}{2}E_{O_2} - E_{In_2O_3} \quad (4)$$

$$\Delta E_{Hads} = E_{H-In_2O_3} - E_{In_2O_3} - \frac{1}{2}E_{H_2} \quad (5)$$

RESULTS AND DISCUSSION

By varying the In precursor, it was possible to synthesize both c-In_2O_3 and h-In_2O_3 polymorphs. As shown in the XRD patterns in **Figure 1a**, the c-In_2O_3 exhibits a main reflection at 30.6°, which is assigned to a (222) lattice plane (JCPDS, NO. 06-0416). The h-In_2O_3 sample shows distinct diffraction peaks at 31.0° and 32.6°, corresponding to the (104) and (110) crystal planes (JCPDS, NO. 22-0336). The morphologies of c-In_2O_3 and h-In_2O_3 were determined by SEM (**Figure S1**) and high-resolution TEM (**Figure 1b-e**). As shown in the TEM images, c-In_2O_3 nanoparticles show polyhedron characteristics with an average particle size around 50 nm and a lattice spacing of 0.29 nm (**Figure 1c**) corresponding to the (222) planes, which is consistent with XRD results showing that c-In_2O_3 mainly exposes the (222) facet. For h-In_2O_3, **Figure S1** and **Figure 1d** show that the as-prepared h-In_2O_3 nanorods have a diameter of 20-50 nm and a length up to 100 nm.[51] The (110) planes of h-In_2O_3 can be identified in **Figure 1e**. Phase-pure c-In_2O_3 and h-In_2O_3 catalysts with different exposed facets provide a unique platform to compare the catalytic performance on different surfaces and thus help build the structure-activity relationship of In_2O_3 catalysts.

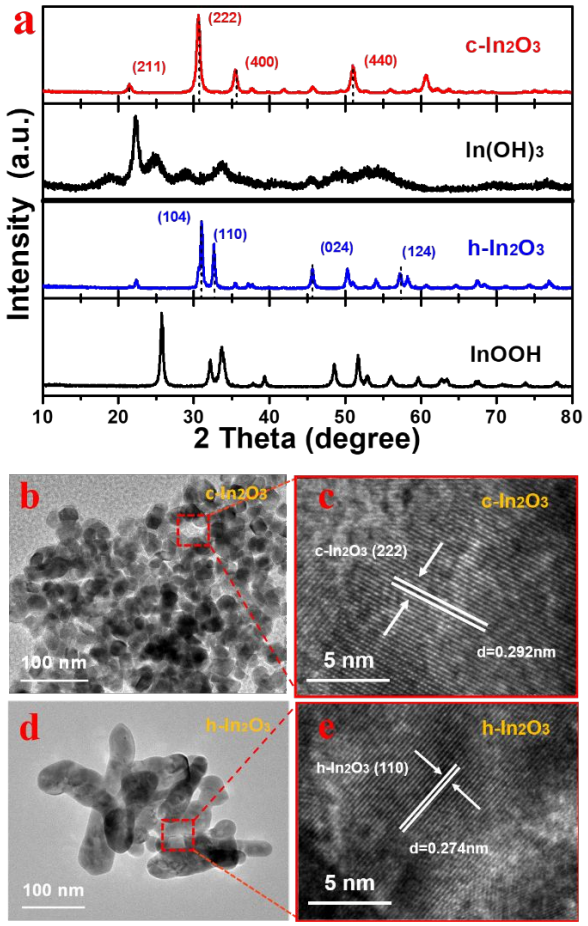

Figure 1. (a) XRD patterns of c-In_2O_3 and h-In_2O_3. (b, c) HRTEM images of c-In_2O_3 and (d, e) HRTEM images of h-In_2O_3.

We next examined the catalytic performance of c-In_2O_3 and h-In_2O_3 in RWGS reaction. As shown in **Figure 2a**, the RWGS rate of c-In_2O_3 is higher than h-In_2O_3 at 450 ℃ (CO selectivity>99%). It is worthy to note that, as the reaction progresses, the activity of the h-In_2O_3 increases gradually, while that of the c-In_2O_3 remains constant, which likely suggests a changing surface structure on h-In_2O_3 but a constant surface structure on c-In_2O_3. After four hours on stream, the CO formation rate of both catalysts are almost the same, which likely suggests that these two catalysts have the same surface structure after four hours. As shown in the XRD patterns in **Figure 2b**, the crystal phase of c-In_2O_3 did not change after four hours of the RWGS reaction, consistent with proposed constant surface structure. While for the h-In_2O_3, almost all the h-In_2O_3

has turned into the cubic phase, suggesting a significant phase transition from h-In_2O_3 to c-In_2O_3 occurred during the RWGS reaction (**Figure S2**)

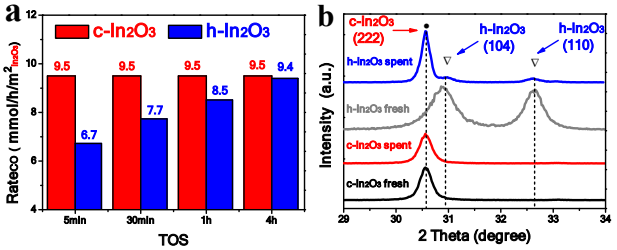

Figure 2. (a) The rate of CO formation over c-In_2O_3 and h-In_2O_3 normalized to the specific surface area and (b) XRD patterns of c-In_2O_3 and h-In_2O_3 (fresh and spent). Reaction conditions: 450℃, TOS = 4h, GHSV = 18000 mL/g/h, H_2/CO_2 = 2, P = 0.1MPa, CO selectivity > 99%.

In order to confirm the crystal phase transition occurred under RWGS conditions, in-situ XRD measurements were performed on h-In_2O_3 at 450℃. As shown in **Figure 3a**, phase transition was firstly observed on the h-In_2O_3 surface, as the reaction proceeds, the reflection at 30.6° corresponding to the (222) crystal plane of c-In_2O_3 grows (**Figure S3**). It is also worthy to note that with longer time on stream, almost all the h-In_2O_3 can turn into the cubic phase, as suggested by the XRD patterns shown in the **Figure 2b**. Furthermore, the morphologies of the spent h-In_2O_3 catalyst were determined by HRTEM. As shown in **Figure 3b**, the nanorod morphology remains after the RWGS reaction at 450℃. The lattice spacings of 0.397nm and 0.292 nm were observed, which correspond to the (012) crystal plane of h-In_2O_3 and the (222) crystal plane of c-In_2O_3, respectively, consistent with the in-situ XRD results confirming the phase transition from h-In_2O_3 to c-In_2O_3.

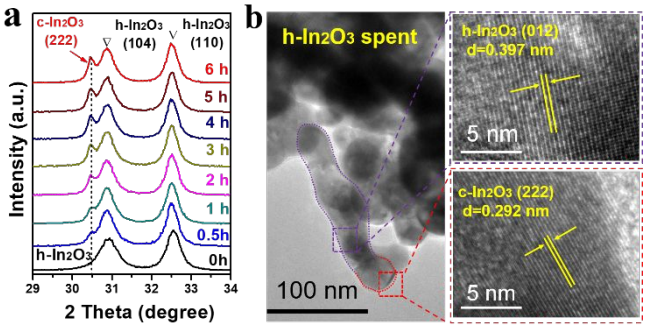

Figure 3. (a) In-situ XRD patterns of h-In_2O_3 during RWGS reaction and (b) HRTEM images of h-In_2O_3 after RWGS reaction. Reaction conditions: 450℃, TOS = 2h, GHSV = 18000 mL/g/h, H_2/CO_2 = 2, P = 0.1MPa.

A series of control experiments were performed to gain insight into the phase transition. As shown in **Figure 4a**, no phase transition was observed with N_2 treatment at 450℃, suggesting the absence of thermally induced phase transition. Similarly, CO_2 treatment did not lead to any detectable phase transition. As shown in **Figure S4**, we determined the thermodynamic phase transition temperature of h-In_2O_3 with in situ XRD and found 550 ℃ was the lowest temperature where thermodynamic phase transition occurs. H_2 treatment in the absence of CO_2 led to full reduction of In_2O_3 to In (0) without any detectable amount of c-In_2O_3. These results suggest that the phase transition (from h-In_2O_3 to c-In_2O_3) occurs only during the RWGS reaction, in which both CO_2 and H_2 are present. Since control experiments eliminate the possibility of thermally induced phase transition, we next focused on possible chemically induced phase transition. As suggested by the XRD results, CO_2 does not react with h-In_2O_3, but H_2 reduces h-In_2O_3 to In (0) which can be oxidized with CO_2 to c-In_2O_3 (due to the thermal stability of the c-In_2O_3) as shown in the XRD results in **Figure 4b**. It is possible that the phase transition occurs through h-In_2O_3 →In (0) →c-In_2O_3. We did not see the presence of In (0) in in-situ XRD under RWGS conditions at 450 ℃, but this does not rule out the possibility of the phase transition going through In (0), since In (0) is molten (amorphous) at 450℃ and might be more rapidly oxidized by CO_2 than the reduction of h-In_2O_3 to In (0). With operando XAS-XRD and in situ TEM, Müller et al. observed that under reaction conditions the structure of the In_2O_3 catalyst is highly dynamic leading to a reductive amorphization and a continuous interconversion between In (0) and crystalline In_2O_3 domains,[62] which provides an explanation of the absence of In(0) diffraction in the in-situ XRD results. To eliminate the possible oxidation of In (0) with trace amount of O_2 in the CO_2 feed, GC analysis was performed simultaneously with the XRD control experiments. As shown in **Figure S5**, CO was observed after exposing In (0) with CO_2 which confirms that CO_2 oxidizes In (0) to c-In_2O_3. It is worthy to note that CO produced through the RWGS reaction can also reduce In_2O_3. However, as shown in **Figure S6a**, H_2 plays a more important role in the reduction, likely because of a much higher partial pressure of H_2 (⩾49%) than CO (⩽7%) under reaction conditions (CO_2 conversion is about 25%). In addition to CO_2, another weak oxidant, H_2O, is also present, as it is generated by the RWGS reaction. However, as shown in **Figure S6b**, H_2O is playing a less import role in oxidizing In (0) to c-In_2O_3, likely due to the higher partial pressure of CO_2 (⩾21%) than that of H_2O (⩽7%). It is worthy to note that there is another possibility that In_2O_x (x<3, another way to indicate the presence of oxygen vacancies) is the intermediate of phase transition at 450℃. If x is very close to 3, we suspect healing the oxygen vacancies with CO_2 regenerates h-In_2O_3. This is most likely what is happening at 300 ℃ based on our subsequent results. At 450 ℃, x is likely much smaller than 3 (when x = 0, In_2O_x = In (0)), healing the oxygen vacancies on In_2O_x before its further reduction to In (0) may generate c-In_2O_3. Right now we cannot rule out any one of these two possibilities. The phase transition provides a possible explanation of the increasing TOF in RWGS at 450℃ due to the phase transition. However, to quantitatively compare the RWGS performance of h-In_2O_3 and c-In_2O_3 and thus build the structure-performance relationship, it is necessary to study the catalysis under conditions where no phase transition occurs.

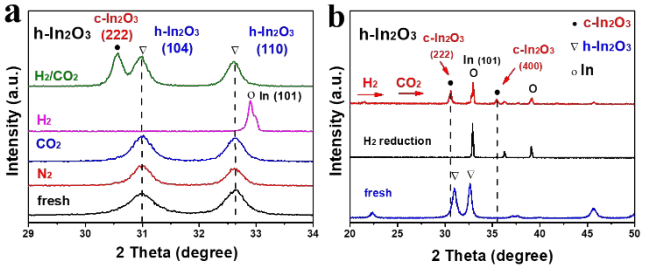

Figure 4. (a, b) XRD patterns of h-In_2O_3 after different gas treatment. Conditions: 450℃， GHSV = 18000 mL/g/h, P = 0.1MPa.

As shown in the in-situ XRD results at various temperatures in **Figure S7** under RWGS reaction condition, the phase transition is much faster at higher temperature. At 500°C, the phase transition is almost complete in about 5 min. While at 400°C, no significant phase transition was observed in 3 hours on stream. So we investigated the catalytic performance of c, h-In_2O_3 catalysts at low temperatures (300-350°C), where no phase transition occurs, as confirmed with the XRD results of the spent catalysts shown in **Figure 5a**. It is also worthy to note that no sintering of the catalysts occurs under these conditions as confirmed by the N_2 adsorption and SEM results (**Table 1** and **Figure S8**). For both c-In_2O_3 and h-In_2O_3, the spent catalysts have the same specific surface area as the fresh ones, c-In_2O_3 (11 m^2/g) and h-In_2O_3 (13 m^2/g), as well as the morphologies determined by SEM (**Figure S8**), which provides an opportunity for an easy comparison of these two catalysts. As shown in **Figure 5b**, the RWGS rate over c-In_2O_3 is about 1.6 times of the h-In_2O_3 within a temperature range of 300 - 350°C, similar to the observed trend at 450°C (**Figure 2a**). As shown in **Figure S9**, the apparent activation energies over c, h-In_2O_3 are different for the RWGS reaction, and the reaction orders for CO formation rate in CO_2 and H_2 were also determined (**Figure S10**).

Table 1. Textural properties of selected samples

Sample		S_{BET} (m^2/g)	Total Pore Volume (cm^3/g)
c-In_2O_3	fresh	11	0.2
	spent	11	0.2
h-In_2O_3	fresh	13	0.2
	spent	13	0.2

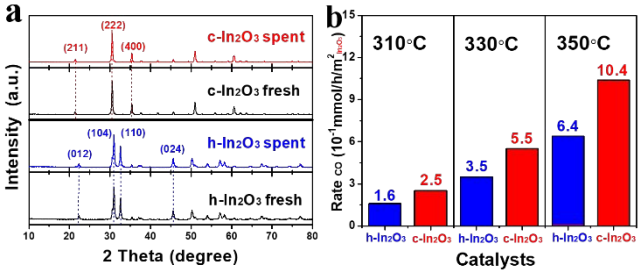

Figure 5. (a) XRD patterns of c-In_2O_3 and h-In_2O_3 (fresh and spent). (b) The rate for CO formation over c-In_2O_3 and h-In_2O_3. Reaction conditions: GHSV = 18000 mL/g/h, H_2/CO_2 = 2, P = 0.1MPa, CO selectivity > 99%.

To gain insight into the catalytic performances over different crystal phases, we investigated c-In_2O_3 and h-In_2O_3 using density functional theory (DFT). DFT calculations suggest that CO_2 activation at oxygen vacancy sites is kinetically inhibited and thus is rate limiting, and that CO_2 adsorption on oxygen vacancies is more favorable on c-In_2O_3 compared to h-In_2O_3. Importantly, H_2 adsorbs more readily over c-In_2O_3 facilitating oxygen vacancy formation. Such reaction mechanisms for CO_2 hydrogenation on In_2O_3 have been studied previously,[38, 40, 44, 48] where surface hydrogen coverage and oxygen vacancy formation have been identified as key players affecting reactivity toward RWGS. CO_2 can be promoted by the formation of oxygen vacancies on In_2O_3, although it has also been shown that CO_2 adsorption is more favorable on the hydroxylated c-In_2O_3(110) surface in the absence of oxygen vacancies.[22] Here, we investigate a reaction mechanism involving CO_2 activation in a surface oxygen vacancy as shown in **Figure 6**. This mechanism begins with H_2 dissociatively adsorbing on the surface (steps a and b), and then reacting with a surface oxygen to form an oxygen vacancy and one water molecule (step c). Subsequently, CO_2 adsorbs on the oxygen vacancy (step d) and heals the vacancy by desorbing CO (step e). We also considered an alternative pathway after the oxygen vacancy formation in which additional H adsorption occurs on the In atom next to the O vacancy (step f) and CO_2 is reduced to CO with the assistance of the additional H atom (step g). The overall reaction can be divided into three parts for further discussion: H adsorption (steps a and b), O vacancy formation (step c), and CO_2 reduction (steps d and e or steps f and g).

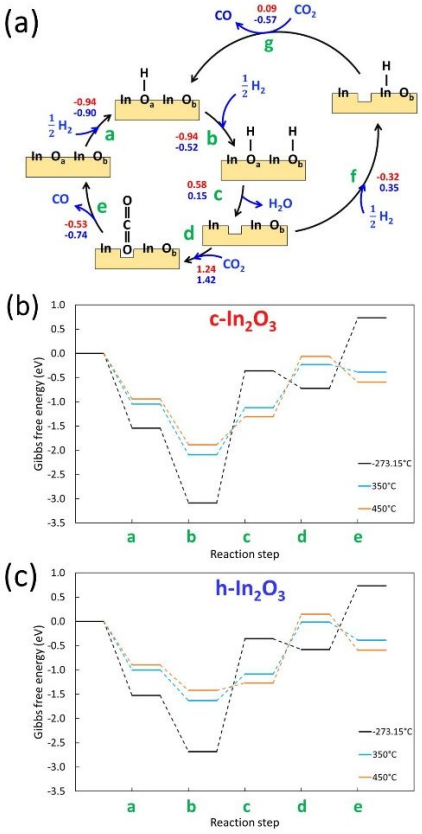

Figure 6. (a) Investigated reaction mechanism for RWGS reaction on In_2O_3 surfaces. O_a represents the most favorable site to form an O vacancy and to adsorb hydrogen atoms, while O_b is the nearest neighbor surface O atom closest to O_a. Reaction Gibbs free energies are computed under the reaction conditions in **Figure 2** with CO_2 conversion of ~0.1% (450°C and partial pressure for CO_2, H_2, CO, and H_2O is 0.56, 1.12, 5.6×10^{-4}, and 5.6×10^{-4} atm, respectively). Energies over c-In_2O_3(111) are shown in red text and over h-In_2O_3(110) in blue text, while the units are in eV. Reaction Gibbs free energy under various reaction temperatures, e.g. -273.15°C, 350°C, and 450°C, on (b) c-In_2O_3(111) and (c) h-In_2O_3(110).

We first computed hydrogen adsorption energies (ΔE_{Hads}) and oxygen vacancy formation energies (ΔE_{Ovac}) on all surface oxygen atom sites. We chose the c-In_2O_3(111) and h-In_2O_3(110) surfaces (**Figure 7**) because they are most prominent XRD features identified in **Figure 1**, and also because these are the most stable surfaces of each polymorph.[57] ΔE_{Ovac} and ΔE_{Hads} for

each site are listed in **Table S1**, which shows that the sites that most favorably adsorb H also most favorably form an O vacancy, as expected. In **Figure 7**, we highlight the most favorable sites for oxygen vacancy formation in blue and the nearest neighbor oxygen atom in green. We take these adjacent sites to be the location of dissociative H_2 adsorption at the onset of the investigated RWGS reaction cycle. The most favorable sites are found to cluster together on the c-In_2O_3(111) surface (i.e., sites 3, 4, and 7 in **Figure 7a**) in agreement with the behavior reported by Albani et al.,[50] whereas the favorable H adsorption sites and are distant from each other on the h-In_2O_3(110) surface (i.e., sites 1, 6, and 7 in **Figure 7c**). We posit that this surface oxygen arrangement facilities H_2 adsorption on c-In_2O_3(111) compared to h-In_2O_3(110), as the most favorable H adsorption sites are in close proximity on c-In_2O_3(111) providing sites for rapid H_2 dissociation and oxygen vacancy formation.

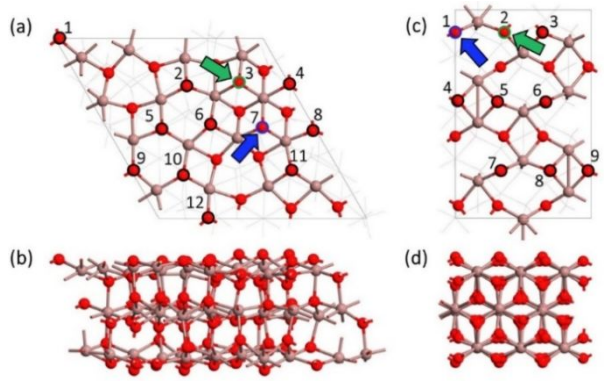

Figure 7. Top/side view of (a)/(b) c-In_2O_3(111) and (c)/(d) h-In_2O_3(110). The blue arrows point to the most favorable site to form an O vacancy and to adsorb a H atom. The green arrows point to the nearest neighboring O atom to the most favorable H adsorption site. (Oxygen is shown in red and indium is shown in brown).

We computed the reaction energy of each step (**Figure 6**) to understand key differences in RWGS activity at 450°C when CO_2 conversion is 0.1%, which was chosen to represent the experimental reaction conditions. The first part of the reaction, H adsorption, exhibits a critical difference in RWGS reactivity between c-In_2O_3 and h-In_2O_3. In step a, both substrates have comparable H binding strengths (at site 7 on the cubic surface and at site 1 on the hexagonal surfaces); however, site 2 on h-In_2O_3(110) binds H less favorably by 0.42 eV compared to site 3 on c-In_2O_3(111). Thus, we expect that dissociative H_2 adsorption will occur more readily over the c-In_2O_3 surface. Another key difference between the polymorphs is evident in the CO_2 reduction sequence, which we consider to be rate determining because CO_2 adsorption (step d) is the most endergonic step under reaction temperatures (e.g, $T \geq 450$°C). According to the reaction Gibbs free energy of step d, c-In_2O_3(111) exhibits stronger CO_2 adsorption than that of h-In_2O_3(110), which leads to higher reactivity because the surface can more readily activate CO_2. In the alternate CO_2 reduction pathway proceeding through steps f and g, CO_2 adsorption over h-In_2O_3(110) is more exergonic compared to c-In_2O_3(111). However, the preceding H adsorption step on the In atom at the oxygen vacancy (step f) is not favorable over h-In_2O_3(110), while it is favorable over c-In_2O_3(111) surface. Furthermore, a high reaction barrier is expected in step g due to the complex geometry rearrangement required for CO_2 to concertedly abstract the adsorbed H atom and desorb CO. These results suggest that RWGS over c-In_2O_3 can be attributed primarily to an enhanced ability to dissociatively adsorb H_2, which in turn enhances the surface's ability to adsorb and activate CO_2.

To investigate the temperature dependence in reactivity, we calculated the reaction Gibbs free energy at various temperatures (i.e., -273.15°C, 310°C, 330°C, 350°C, and 450°C), which are illustrated in **Figure 6b** and **6c** and listed in **Table S2** and **Table S3** for c-In_2O_3 and h-In_2O_3, respectively. We found that the rate determining step changes with temperature on c-In_2O_3. At low temperature (e.g. $T \leq 350$°C), the desorption of water (step c) becomes more endergonic than CO_2 adsorption (step d). This phenomenon is not observed on h-In_2O_3 under the reaction temperature range, but is expected at lower temperature, since step c dominates the reaction rate at -273.15°C. This suggests that water release and oxygen vacancy formation can become rate limiting at low temperatures. We also consider the reaction Gibbs free energy when partial pressures of the chemicals are all at 1 atm (**Table S4** and **S5**), which shows that the transition of the rate determining step from H_2O desorption to CO_2 adsorption occurs between 330°C and 350°C on h-In_2O_3 and between 350°C and 450°C on c-In_2O_3 at higher conversions when the partial pressures of reactants and products are comparable.

We employed the Dudarev's DFT+U formalism with a U value of 7 eV on In d states to test the sensitivity of these results with respect to known GGA deficiencies in handling localized states in oxides (**Table S6**).[60-61] The energy of steps a, b, and c show only slight changes. CO_2 adsorption on the O vacancy, step d, becomes comparable on cubic and hexagonal surfaces, while step e becomes 0.43 and 0.53 eV more favorable on c-In_2O_3 and h-In_2O_3, respectively, compared to the DFT-PBE values without U correction. A significant change in energy is observed for step f (increasing for c-In_2O_3 and decreasing for h-In_2O_3) and step g (decreasing on both surfaces) due to the shift in energy of the surface with one O vacancy and one adsorbed H atom, as expected because the surface is reduced and exhibits localized electrons. Although both steps f and g are favorable on hexagonal-In_2O_3, we suggest that the high barrier in step g may block this path as discussed above.

The DFT+U calculations underscore the importance of hydrogen adsorption as the key difference between the two polymorphs, which is a trend that does not change with application of the +U correction. Conversely, the CO_2 adsorption energy becomes comparable on the two polymorphs with the +U correction, suggesting that this step may exhibit similar energetics over both surfaces. Hence, we hypothesize that differences in hydrogen adsorption, rather than in CO_2 adsorption energy, are primarily responsible for the difference in RWGS performance. Note that although here we investigated CO_2 adsorption in oxygen vacancies, this conclusion would also hold for CO_2 adsorption on pristine surfaces induced by surface hydrogenation, as proposed by Posada-Borbón and Grönbeck,[22] where the polymorph that more readily adsorbs hydrogen will also more readily activate CO_2 because it will exhibit higher hydrogen coverage. Investigation of alternative mechanisms that do not involve CO_2 activation at an oxygen vacancy, but rather on pristine surfaces in the presence of high hydrogen coverage, are underway.

To verify this conclusion experimentally, we studied chemisorption properties of c-In_2O_3 and h-In_2O_3 by H_2-TPR and CO_2-TPD. The H_2-TPR profiles of both c-In_2O_3 and h-In_2O_3 are shown in **Figure 8a**. The reduction peaks above 450°C

correspond to the reduction of bulk In_2O_3, while those below 350℃ represent the reduction of the catalyst surface, i.e., the formation of surface oxygen vacancies.[38, 40] Compared to the reduction temperature of h-In_2O_3 around 300℃, the reduction of c-In_2O_3 shifts to lower temperature (230℃), suggesting that the generation of oxygen vacancy is much easier on c-In_2O_3 than the h-In_2O_3. Furthermore, by the estimated H_2 consumption areas on the TPR profiles, we expect the concentration of the c-In_2O_3 surface oxygen vacancy is higher than that of h-In_2O_3, where the c-In_2O_3 consumes more H_2 than h-In_2O_3 according to the **Table S7.** This observation agrees with the DFT results and XPS results in **Figure S11**. The O1s core level spectra are displayed in **Figure S11a** where the peak at 531.4 eV is assigned to O atoms next to a defect (O defect).[40, 46, 48] As shown in **Table S8**, the concentration of the c-In_2O_3 (fresh and spent) surface oxygen vacancy is higher than that of h-In_2O_3, which means on the c-In_2O_3 surface, there are more active sites than h-In_2O_3. Furthermore, CO_2 adsorption properties of c-In_2O_3 and h-In_2O_3 surface were investigated by CO_2 temperature-programed desorption. CO_2-TPD profiles in **Figure 8b** can be divided into two regions:100-150 and 400-550℃, corresponding to the physically adsorbed CO_2 and chemically adsorbed CO_2 on the H_2 induced oxygen vacancy sites (O_v), respectively.[35, 37] To study the role of oxygen vacancies, the effluent products were determined during CO_2-TPD by mass spectrometry (TPD-MS). As shown in **Figure S12**, a large amount of CO was observed when c-In_2O_3 with O_v was exposed to CO_2 at 300℃, indicating that the O_v can dissociate CO_2 under reaction conditions. Clearly, the desorption profile of c-In_2O_3 resembles that of h-In_2O_3 in the whole temperature range, except the area of CO_2 chemisorption peak is bigger and shifted towards higher temperatures, it indicates that the CO_2 chemisorption at the oxygen vacancy sites on c-In_2O_3 surface is much stronger than that on h-In_2O_3. We further investigated the turn-over frequency (TOF) of CO formation over c-In_2O_3 and h-In_2O_3, where the number of active sites were determined by CO_2-TPD, and found the TOF on c-In_2O_3 is slightly higher (~ 1.1 times) than that of h-In_2O_3 (**Figure S13**). These results are consistent with the DFT calculations, which indicates that c-In_2O_3 exhibits a higher RWGS rate than h-In_2O_3 due to its (1) facile formation of more oxygen vacancies (active sites), and (2) enhanced ability to adsorb and activate CO_2 on the oxygen vacancies.

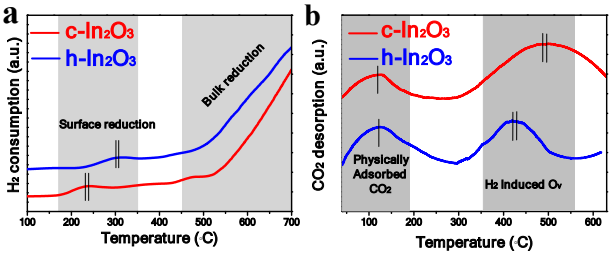

Figure 8. (a) H_2-TPR and (b) CO_2-TPD profiles of c-In_2O_3 and h-In_2O_3 catalysts

CONCLUSIONS

In_2O_3 with different crystal phases were prepared and evaluated for RWGS reaction. Under the high temperature conditions (450℃), c-In_2O_3 shows stable catalytic performance, while h-In_2O_3 shows an increasing catalytic activity due to the phase transition from h-In_2O_3 to c-In_2O_3. In-situ XRD results suggest that the crystal phase transition occurs through two steps, firstly H_2 reduces h-In_2O_3 to In (0) or In_2O_x, and then CO_2 oxidizes In (0) or In_2O_x to c-In_2O_3. During the low temperature reaction (300-350℃), both h-In_2O_3 and c-In_2O_3 are highly selective toward CO (>99%) over CH_4, while c-In_2O_3 exhibits about 1.6 times higher rate (per surface area) than that of h-In_2O_3. DFT simulations demonstrate that the higher RWGS rate over c-In_2O_3 can be attributed to (1) an enhanced ability to dissociatively adsorb H_2, resulting from favorable surface O arrangement and (2) an enhanced ability to adsorb and activate CO_2. Further surface analyses verify that it is easier to adsorb H_2 and to form oxygen vacancies on the surface of c-In_2O_3 and that these oxygen vacancies adsorb CO_2 stronger than on the h-In_2O_3 surface. Our results demonstrate the importance of crystal structure for catalytic performance. These results may be extend to other catalytic systems to design catalysts for important chemical reactions.

ASSOCIATED CONTENT

Supporting Information.
SEM images, XRD results, XPS results, additional kinetic and DFT data.

AUTHOR INFORMATION

Corresponding Author

* Guanghui Zhang: gzhang@dlut.edu.cn;

* Xinwen Guo: guoxw@dlut.edu.cn;

* Chunshan Song: csong@psu.edu.

Author Contributions

The manuscript was written through contributions of all authors. All authors have given approval to the final version of the manuscript. ‡ J.W. and C.-Y.L. contributed equally to the work.

Notes

The authors declare no competing financial interest.

ACKNOWLEDGMENT

This work was financially supported by the National Key Research and Development Program of China (2016YFB0600902-4), National Natural Science Foundation of China (21902019), Fundamental Research Funds for Central Universities (DUT18RC(3)057) and the Pennsylvania State University. C.-Y.L. and T.P.S. acknowledge startup funding from Rice University.

REFERENCES

1. Auffhammer, M.; Carson, R. T. Forecasting the path of China's CO_2 emissions using province-level information. *J. Environ. Econ. Manag.* **2008,** *55,* 229-247.
2. Tahir, M.; Amin, N. S. Advances in visible light responsive titanium oxide-based photocatalysts for CO_2 conversion to hydrocarbon fuels. *Energ. Convers. Manag.* **2013,** *76,* 194-214.
3. Dorner, R. W.; Hardy, D. R.; Williams, F. W.; Willauer, H. D. Heterogeneous catalytic CO_2 conversion to value-added hydrocarbons. *Energy Environ. Sci.* **2010,** *3,* 884-890.
4. Guo, L. S.; Sun, J.; Ge, Q. J.; Tsubaki, N. Recent advances in direct catalytic hydrogenation of carbon dioxide to valuable C_2^+ hydrocarbons. *J. Mater. Chem. A.* **2018, 6**, 23244-23262.
5. Tackett, B. M.; Gomez, E.; Chen, J. G. Net reduction of CO_2 via its thermocatalytic and electrocatalytic transformation reactions in standard and hybrid processes. *Nat. Catal.* **2019,** *2,* 381-386.
6. Centi, G.; Quadrelli, E. A.; Perathoner, S. Catalysis for CO_2 conversion: a key technology for rapid introduction of renewable

energy in the value chain of chemical industries. *Energy Environ. Sci.* **2013,** *6,* 1711-1731.
7. Daza, Y. A.; Kuhn, J. N. CO_2 conversion by reverse water gas shift catalysis: comparison of catalysts, mechanisms and their consequences for CO_2 conversion to liquid fuels. *RSC Adv.* **2016,** *6,* 49675-49691.
8. Porosoff, M. D.; Yan, B.; Chen, J. G. Catalytic reduction of CO_2 by H_2 for synthesis of CO, methanol and hydrocarbons: challenges and opportunities. *Energy Environ. Sci.* **2016,** *9,* 62-73.
9. Barreiro, M. M.; Maroño, M.; Sánchez, J. M. Hydrogen permeation through a Pd-based membrane and RWGS conversion in H_2/CO_2, $H_2/N_2/CO_2$ and $H_2/H_2O/CO_2$ mixtures. *Int. J. Hydrog. Energy.* **2014,** *39,* 4710-4716.
10. Chen, X.; Su, X.; Duan, H.; Liang, B.; Huang, Y.; Zhang, T. Catalytic performance of the Pt/TiO_2 catalysts in reverse water gas shift reaction: Controlled product selectivity and a mechanism study. *Catal. Today.* **2017,** *281,* 312-318.
11. Goguet, A.; Meunier, F.; Breen, J.; Burch, R.; Petch, M.; Faurghenciu, A. Study of the origin of the deactivation of a Pt/CeO_2 catalyst during reverse water gas shift (RWGS) reaction. *J. Catal.* **2004,** *226,* 382-392.
12. Kim, S. S.; Lee, H. H.; Hong, S. C. A study on the effect of support's reducibility on the reverse water-gas shift reaction over Pt catalysts. *Appl. Catal. A: Gen.* **2012**, *423-424,* 100-107.
13. Liang, B.; Duan, H.; Su, X.; Chen, X.; Huang, Y.; Chen, X.; Delgado, J. J.; Zhang, T. Promoting role of potassium in the reverse water gas shift reaction on Pt/mullite catalyst. *Catal. Today*. **2017,** *281,* 319-326.
14. Liu, Y.; Li, Z.; Xu, H.; Han, Y. Reverse water–gas shift reaction over ceria nanocube synthesized by hydrothermal method. *Catal. Comun.* **2016,** *76,* 1-6.
15. Ro, I.; Sener, C.; Stadelman, T. M.; Ball, M. R.; Venegas, J. M.; Burt, S. P.; Hermans, I.; Dumesic, J. A.; Huber, G. W. Measurement of intrinsic catalytic activity of Pt monometallic and Pt-MoO_x interfacial sites over visible light enhanced $PtMoO_x/SiO_2$ catalyst in reverse water gas shift reaction. *J. Catal.* **2016,** *344,* 784-794.
16. Sun, F. M.; Yan, C. F.; Wang, Z. D.; Guo, C. Q.; Huang, S. L. Ni/Ce–Zr–O catalyst for high CO_2 conversion during reverse water gas shift reaction (RWGS). *Int. J. Hydrog. Energy.* **2015,** *40,* 15985-15993.
17. Wang, L.; Liu, H.; Chen, Y.; Yang, S. Reverse water–gas shift reaction over co-precipitated Co–CeO_2 catalysts: Effect of Co content on selectivity and carbon formation. *Int. J. Hydrog. Energy.* **2017,** *42,* 3682-3689.
18. Yang, L.; Pastor-Pérez, L.; Gu, S.; Sepúlveda-Escribano, A.; Reina, T. R. Highly efficient Ni/CeO_2-Al_2O_3 catalysts for CO_2 upgrading via reverse water-gas shift: Effect of selected transition metal promoters. *Appl. Catal. B: Environ.* **2018,** *232,* 464-471.
19. Zhang, X.; Zhu, X.; Lin, L.; Yao, S.; Zhang, M.; Liu, X.; Wang, X.; Li, Y. W.; Shi, C.; Ma, D. Highly Dispersed Copper over β-Mo_2C as an Efficient and Stable Catalyst for the Reverse Water Gas Shift (RWGS) Reaction. *ACS Catal.* **2016,** *7,* 912-918.
20. Zonetti, P. C.; Letichevsky, S.; Gaspar, A. B.; Sousa-Aguiar, E. F.; Appel, L. G. The $NixCe_{0.75}Zr_{0.25-x}O_2$ solid solution and the RWGS. *Appl. Catal. A: Gen.* **2014,** *475,* 48-54.
21. Bielz, T.; Lorenz, H.; Amann, P.; Klötzer, B.; Penner, S., Water−Gas Shift and Formaldehyde Reforming Activity Determined by Defect Chemistry of Polycrystalline In_2O_3. *J. Phys. Chem. C*. **2011,** *115,* 6622-6628.
22. Posada, -B. A.; Grönbeck, H., CO_2 adsorption on hydroxylated In_2O_3(110). *Phys. Chem. Chem. Phys.* **2019,** *21,* 21698-21708.
23. Sun, Q.; Ye, J.; Liu, C. J.; Ge, Q. F. In_2O_3 as a promising catalyst for CO_2 utilization: A case study with reverse water gas shift over In_2O_3. *Greenh. Gases.* **2014,** *4,* 140-144.
24. Wang, W.; Zhang, Y.; Wang, Z.; Yan, J. M.; Ge, Q. F.; Liu, C. J. Reverse water gas shift over In_2O_3 –CeO_2 catalysts. *Catal. Today.* **2016,** *259,* 402-408.
25. Rodriguez, J. A.; Liu, P.; Stacchiola, D. J.; Senanayake, S. D.; White, M. G.; Chen, J. G. Hydrogenation of CO_2 to Methanol: Importance of Metal–Oxide and Metal–Carbide Interfaces in the Activation of CO_2. *ACS Catal.* **2015,** *5,* 6696-6706.
26. Dietz, L.; Piccinin, S.; Maestri, M. Mechanistic Insights into CO_2 Activation via Reverse Water–Gas Shift on Metal Surfaces. J. Phys. Chem. C. **2015,** *119,* 4959-4966.
27. Aitbekova, A.; Wu, L.; Wrasman, C. J.; Boubnov, A.; Hoffman, A. S.; Goodman, E. D.; Bare, S. R.; Cargnello, M. Low-Temperature Restructuring of CeO_2-Supported Ru Nanoparticles Determines Selectivity in CO_2 Catalytic Reduction. *J. Am. Chem. Soc.* **2018,** *140,* 13736-13745.
28. Kattel, S.; Liu, P.; Chen, J. G. Tuning Selectivity of CO_2 Hydrogenation Reactions at the Metal/Oxide Interface. *J. Am. Chem. Soc.* **2017,** *139,* 9739-9754.
29. Li, W.; Zhang, G.; Jiang, X.; Liu, Y.; Zhu, J.; Ding, F.; Liu, Z.; Guo, X.; Song, C. CO_2 Hydrogenation on Unpromoted and M-Promoted Co/TiO_2 Catalysts (M = Zr, K, Cs): Effects of Crystal Phase of Supports and Metal–Support Interaction on Tuning Product Distribution. *ACS Catal.* **2019,** *9,* 2739-2751.
30. Matsubu, J. C.; Yang, V. N.; Christopher, P. Isolated metal active site concentration and stability control catalytic CO_2 reduction selectivity. *J. Am. Chem. Soc.* **2015,** *137,* 3076-84.
31. Samson, K.; Śliwa, M.; Socha, R. P.; Góra, M. K.; Mucha, D.; Rutkowska-Zbik, D.; Paul, J. F.; Ruggiero, M. M.; Grabowski, R.; Słoczyński, J. Influence of ZrO_2 Structure and Copper Electronic State on Activity of Cu/ZrO_2 Catalysts in Methanol Synthesis from CO_2. *ACS Catal.* **2014,** *4,* 3730-3741.
32. Kim, A.; Sanchez, C.; Patriarche, G.; Ersen, O.; Moldovan, S.; Wisnet, A.; Sassoye, C.; Debecker, D. P., Selective CO_2 methanation on Ru/TiO_2 catalysts: unravelling the decisive role of the TiO_2 support crystal structure. *Catal. Sci. Technol.* **2016,** *6,* 8117-8128.
33. Liu, J. X.; Su, H. Y.; Sun, D. P.; Zhang, B. Y.; Li, W. X., Crystallographic dependence of CO activation on cobalt catalysts: HCP versus FCC. *J Am Chem Soc*. **2013,** *135,* 16284-16287.
34. Lyu, S.; Wang, L.; Zhang, J.; Liu, C.; Sun, J.; Peng, B.; Wang, Y.; Rappé, K. G.; Zhang, Y.; Li, J.; Nie, L. Role of Active Phase in Fischer–Tropsch Synthesis: Experimental Evidence of CO Activation over Single-Phase Cobalt Catalysts. *ACS Catal.* **2018,** *8,* 7787-7798.
35. Dou, M.; Zhang, M.; Chen, Y.; Yu, Y. Theoretical insights into the surface structure of In_2O_3 (1 1 0) surface and its effect on methanol synthesis from CO_2 hydrogenation. *Comput. Theor. Chem.* **2018,** *1126,* 7-15.
36. Frei, M. S.; Capdevila-Cortada, M.; García-Muelas, R.; Mondelli, C.; López, N.; Stewart, J. A.; Curulla Ferré, D.; Pérez-Ramírez, J. Mechanism and microkinetics of methanol synthesis via CO_2 hydrogenation on indium oxide. *J. Catal.* **2018,** *361,* 313-321.
37. García-Trenco, A.; Regoutz, A.; White, E. R.; Payne, D. J.; Shaffer, M. S. P.; Williams, C. K. PdIn intermetallic nanoparticles for the Hydrogenation of CO_2 to Methanol. *Appl. Catal. B: Environ.* **2018,** *220,* 9-18.
38. Martin, O.; Martin, A. J.; Mondelli, C.; Mitchell, S.; Segawa, T. F.; Hauert, R.; Drouilly, C.; Curulla-Ferre, D.; Perez-Ramirez, J. Indium Oxide as a Superior Catalyst for Methanol Synthesis by CO_2 Hydrogenation. *Angew. Chem. Int. Ed.* **2016,** *55,* 6261-6265.
39. Richard, A. R.; Fan, M. Low-Pressure Hydrogenation of CO_2 to CH_3OH Using Ni-In-Al/SiO_2 Catalyst Synthesized via a Phyllosilicate Precursor. *ACS Catal.* **2017,** *7, 5679-5692.*
40. Rui, N.; Wang, Z.; Sun, K.; Ye, J.; Ge, Q.; Liu, C. J. CO_2 hydrogenation to methanol over Pd/In_2O_3: effects of Pd and oxygen vacancy. *Appl. Catal. B: Environ.* **2017,** *218,* 488-497.
41. Snider, J. L.; Streibel, V.; Hubert, M. A.; Choksi, T. S.; Valle, E.; Upham, D. C.; Schumann, J.; Duyar, M. S.; Gallo, A.; Abild-Pedersen, F.; Jaramillo, T. F. Revealing the Synergy between Oxide and Alloy Phases on the Performance of Bimetallic In–Pd Catalysts for CO_2 Hydrogenation to Methanol. *ACS Catal.* **2019,** *9,* 3399-3412.
42. Sun, K.; Fan, Z.; Ye, J.; Yan, J.; Ge, Q. F.; Li, Y.; He, W.; Yang, W.; Liu, C. J. Hydrogenation of CO_2 to methanol over In_2O_3 catalyst. *J.CO_2 Util.* **2015,** *12,* 1-6.
43. Ye, J.; Liu, C.; Ge, Q. F. DFT Study of CO_2 Adsorption and Hydrogenation on the In_2O_3 Surface. *J. Phys. Chem. C.* **2012,** *116,* 7817-7825.
44. Ye, J.; Liu, C.; Mei, D.; Ge, Q. F. Active Oxygen Vacancy Site for Methanol Synthesis from CO_2 Hydrogenation on In_2O_3(110): A DFT Study. *ACS Catal.* **2013,** *3,* 1296-1306.
45. Ye, J.; Liu, C. J.; Mei, D.; Ge, Q. F. Methanol synthesis from CO_2 hydrogenation over a $Pd4/In_2O_3$ model catalyst: A combined DFT and

kinetic study. *J. Catal.* **2014,** *317,* 44-53.
46. Dang, S.; Gao, P.; Liu, Z.; Chen, X.; Yang, C.; Wang, H.; Zhong, L.; Li, S.; Sun, Y. Role of zirconium in direct CO_2 hydrogenation to lower olefins on oxide/zeolite bifunctional catalysts. *J. Catal.* **2018,** *364,* 382-393.
47. Gao, J.; Jia, C.; Liu, B., Direct and selective hydrogenation of CO_2 to ethylene and propene by bifunctional catalysts. *Catal. Sci. Technol.* **2017,** *7,* 5602-5607.
48. Gao, P.; Li, S.; Bu, X.; Dang, S.; Liu, Z.; Wang, H.; Zhong, L.; Qiu, M.; Yang, C.; Cai, J.; Wei, W.; Sun, Y. Direct conversion of CO_2 into liquid fuels with high selectivity over a bifunctional catalyst. *Nat. Chem.* **2017,** *9,* 1019-1024.
49. Su, J.; Wang, D.; Wang, Y.; Zhou, H.; Liu, C.; Liu, S.; Wang, C.; Yang, W.; Xie, Z.; He, M. Direct Conversion of Syngas into Light Olefins over Zirconium-Doped Indium(III) Oxide and SAPO-34 Bifunctional Catalysts: Design of Oxide Component and Construction of Reaction Network. *ChemCatChem* **2018***, 10,* 1536-1541.
50. Albani, D.; Capdevila, C. M.; Vile, G.; Mitchell, S.; Martin, O.; Lopez, N.; Perez-Ramirez, J. Semihydrogenation of Acetylene on Indium Oxide: Proposed Single-Ensemble Catalysis. *Angew. Chem. Int. Ed.* **2017,** *56,* 10755-10760.
51. Xu, J.; Chen, Y.; Shen, J., Ethanol sensor based on hexagonal indium oxide nanorods prepared by solvothermal methods. *Mater. Lett.* **2008***, 62,* 1363-1365.
52. Kresse, G.; Furthmu¨ller, J. Efficient iterative schemes for ab initio total-energy calculations using a plane-wave basis set. *Phys. Rev. B.* **1996,** *54,* 11169-11186.
53. Blochl, P. E., Projector augmented-wave method. *Phys. Rev. B.* **1994,** *50,* 17953-17979.
54. Kresse, G.; Joubert, B. From ultrasoft pseudopotentials to the projector augmented-wave method. *Phys. Rev. B.***1999,** *59,* 1758-1775.
55. Perdew, J. P.; Burke, K.; Ernzerhof, M. Generalized Gradient Approximation Made Simple. *Phys. Rev. Lett.* **1996,** *77,* 3865-3868.
56. Monkhorst, H. J.; Pack, J. D. Special points for Brillouin-zone integrations. *Phy. Rev. B.* **1976,** *13,* 5188-5192.
57. Walsh, A.; Catlow, C. R. A. Structure, stability and work functions of the low index surfaces of pure indium oxide and Sn-doped indium oxide (ITO) from density functional theory. *J. Mater. Chem.* **2010,** *20,* 10438-10444.
58. Grimme, S.; Antony, J.; Ehrlich, S.; Krieg, H. A consistent and accurate ab initio parametrization of density functional dispersion correction (DFT-D) for the 94 elements H-Pu. *J. Chem. Phys.* **2010,** *132,* 154104.
59. Hinnemann, B.; Carter, E. A. Adsorption of Al, O, Hf, Y, Pt, and S Atoms on r-Al_2O_3(0001). *J. Phys. Chem. C.* **2007,** *111,* 7105-7126.
60. Dudarev, S. L.; Botton, G. A.; Savrasov, S. Y.; Humphreys, J. C.; Sutton, P. A. Electron-energy-loss spectra and the structural stability of nickel oxide An LSDA1U study. *Phys. Rev. B.* **1998,** *57,* 1505-1509.
61. Erhart, P.; Klein, A.; Egdell, R. G.; Albe, K. Band structure of indium oxide: Indirect versus direct band gap. P*hys. Rev. B.* **2007,** *75.* 153205.
62. Tsoukalou, A.; Abdala, P. M.; Stoian, D.; Huang, X.; Willinger, M. G.; Fedorov, A.; Muller, C. R. The Structural Evolution and Dynamics of an In_2O_3 Catalyst for CO_2 Hydrogenation to Methanol: An Operando XAS-XRD and In Situ TEM Study. *J. Am. Chem. Soc.* **2019,** *141,* 13497−13505.

SYNOPSIS TOC